Electronic and optical properties of $Mg_xZn_{1-x}O$ and $Cd_xZn_{1-x}O$ from *ab initio* calculations

2011 New J. Phys. 13 085012

(http://iopscience.iop.org/1367-2630/13/8/085012)

New Journal of Physics
The open-access journal for physics

Electronic and optical properties of $Mg_xZn_{1-x}O$ and $Cd_xZn_{1-x}O$ from *ab initio* calculations

André Schleife[1,2], Claudia Rödl, Jürgen Furthmüller and Friedhelm Bechstedt

Institut für Festkörpertheorie und -optik and European Theoretical Spectroscopy Facility (ETSF), Friedrich-Schiller-Universität, Max-Wien-Platz 1, 07743 Jena, Germany
E-mail: a.schleife@llnl.gov

New Journal of Physics **13** (2011) 085012 (24pp)
Received 2 April 2011
Published 16 August 2011
Online at http://www.njp.org/
doi:10.1088/1367-2630/13/8/085012

Abstract. Isostructural and heterostructural pseudobinary $Mg_xZn_{1-x}O$ and $Cd_xZn_{1-x}O$ alloys are studied by combining the wurtzite and the rocksalt polymorphs within a cluster expansion. The computationally demanding calculation of the quasiparticle electronic structure has been achieved for all cluster cells of the expansion using the recently developed HSE03 + G_0W_0 scheme. These results are used to compute the configurational averages for the fundamental band gaps and the densities of states. A strongly nonlinear behavior of the band gaps is observed and it is quantified by means of the corresponding bowing parameters for both material systems. In order to calculate the macroscopic dielectric functions, including excitonic and local-field effects for iso- and heterostructural $Mg_xZn_{1-x}O$ alloys as well as wurtzite (wz) $Cd_xZn_{1-x}O$, the Bethe–Salpeter equation has been solved for each of the corresponding clusters. The respective configurational averages indicate that the composition-dependent variation in the exciton peaks allows conclusions on the alloy composition and preparation conditions.

[1] Author to whom any correspondence should be addressed.
[2] Current address: Condensed Matter and Materials Division, Lawrence Livermore National Laboratory, Livermore, CA 94550, USA.

Contents

1. Introduction

In the context of modern optoelectronics, oxide materials experience an ongoing boom [1], which is mostly triggered by their impact on green-energy [2, 3], intelligent-materials [4] and transparent-electronics [5, 6] applications. An efficient combination of electrical and optical components is desirable, for instance, to exponentiate the signal processing speed in networking technology. For different group-II oxides, in addition to their large fundamental band gaps [7], a certain conductivity has been achieved by means of intentional [8–10] as well as unintentional [11, 12] *n*-doping. Consequently, these materials combine transparency in the optical spectral range and electrical conductivity under ambient conditions. As transparent conducting oxides (TCOs), they are currently of particular interest for the so-called 'transparent electronics' or 'oxide electronics' [13, 14].

Since their fundamental band gaps span a range of several electronvolts, MgO, ZnO and CdO are interesting as alloys or heterostructures, especially when going beyond the better understanding of materials towards *tailoring* certain structural or electronic properties for different applications [14–18]. It is confirmed experimentally [15, 16, 19] that the absorption onset can be tuned from about 3.4 eV in wurtzite (wz) ZnO up to ≈ 4.4 eV in $Mg_xZn_{1-x}O$, which makes the ultraviolet spectral region accessible. Conversely, pseudobinary $Cd_xZn_{1-x}O$ alloys feature smaller gaps, rendering them suitable for devices that operate in the visible spectral range [17, 20, 21].

However, in contrast to many nitride-based alloy systems, the combination of the group-II oxides in alloys and heterostructures is more difficult, since ZnO crystallizes in the hexagonal wz structure under ambient conditions, whereas the most stable polymorph of MgO and CdO is the rocksalt (rs) one [22, 23]. The composition of such a heterostructural

alloy system can strongly depend on the preparation (growth, deposition, etc) conditions. While the thermodynamic properties and structural composition of iso- and heterostructural $Mg_xZn_{1-x}O$ and $Cd_xZn_{1-x}O$ alloys have been investigated, taking into account different preparation conditions [24], these questions will be answered for the electronic structure and optical properties in this work. Thus, understanding the evolution of the fundamental band gap with varying composition, crystal structure and preparation conditions is of great fundamental interest as well as practical relevance. In particular, band-gap bowing, i.e. the deviation of the fundamental band gap from a linear behavior with varying temperature or composition of the alloy system, is important. Since the definition of a band gap for an alloy system can be more involved [25], integrated quantities, such as the densities of states (DOSs) or the dielectric functions (DFs), are also investigated in this work.

Here, a combination of modern parameter-free theoretical-spectroscopy techniques and a cluster expansion method is used to explore the electronic structure and optical properties of iso- and heterostructural $Mg_xZn_{1-x}O$ and $Cd_xZn_{1-x}O$ alloys. In section 2, the methodology is described and the computational details are given. The quasiparticle (QP) electronic structure of the alloys is discussed in detail in section 3, followed by an investigation of the optical properties in section 4. Throughout, the computed results are discussed with respect to the available experimental data. Finally, the paper is summarized in section 5.

2. Theoretical and computational approach

2.1. Cluster expansion and cluster fractions

In this paper, theoretical approaches are employed based on a cluster expansion method that has been developed to describe isostructural as well as heterostructural pseudobinary alloys of the type $A_xB_{1-x}C$. While the approach is briefly summarized in the following, it is described in greater detail in [24, 26–29].

An isostructural, pseudobinary alloy $A_xB_{1-x}C$ consists of N atoms of type C on the anion sub-lattice and a total of N atoms of type A and B on the cation sub-lattice. For the cluster expansion, the macroscopic alloy is divided into M clusters, each of which consists of $2n$ atoms (n anions and n cations) [24, 26, 30, 31]. Consequently, the total numbers of cations and anions is $N = nM$. Due to the symmetry of the crystal lattice, all possible clusters can be grouped into $J+1$ different classes. Each class $j\,(j = 0, \ldots, J)$ comprises g_j clusters of the same total energy ε_j. The number of cations of species A in each class is denoted by n_j.

The macroscopic alloy is built of a set of $\{M_0, M_1, \ldots, M_J\}$ clusters. Hence, a single class j contributes with its cluster fraction $x_j = M_j/M$. Since the x_j describe the statistical weights of all clusters, it holds that $\sum_{j=0}^{J} x_j = 1$.

For both the rs and the wz polymorphs of the oxides studied in this work, 16-atom supercells ($n = 8$) are used to simulate the clusters [24, 30]. Thus, 256 clusters occur in total for each material system; they can be grouped into $J+1 = 22$ (wz) or $J+1 = 16$ (rs) classes due to their point-group symmetries. More specifically, the atomic geometries described in [24] are employed in this work.

Within this framework any property P of the macroscopic alloy is connected to the respective properties P_j of the individual clusters via the Connolly–Williams formula [31, 32],

$$P(x, T) = \sum_{j=0}^{J} x_j(x, T)\, P_j. \tag{1}$$

Fluctuations around the configurational averages can be described via the mean-square deviations,

$$\Delta P(x,T) = \sqrt{\sum_{j=0}^{J} x_j(x,T)\, P_j^2 - P^2(x,T)}. \tag{2}$$

Since the weights $x_j(x,T)$ can depend on the composition x of the alloy as well as the temperature T, it is possible to account for the influence of different preparation conditions [24]. In this work, three different situations are identified:

1. The thermodynamic equilibrium is described by cluster fractions that lead to a minimum of the Helmholtz free energy $F(x,T)$. In this case, the so-called generalized quasichemical approximation (GQCA), the weights are given by
$$x_j^{\mathrm{GQCA}}(x,T) = \frac{g_j \eta^{n_j}\, \mathrm{e}^{-\beta\Delta\varepsilon_j}}{\sum_{j'=0}^{J} g_{j'} \eta^{n_{j'}}\, \mathrm{e}^{-\beta\Delta\varepsilon_{j'}}}, \tag{3}$$
where $\beta = 1/k_{\mathrm{B}}T$, $\Delta\varepsilon_j$ is the excess energy of cluster j (see [24, 31] for the definition), and η is determined by minimizing $F(x,T)$ under the constraint $\sum_{j=0}^{J} n_j x_j = nx$ [24, 31].
2. Within the strict-regular solution (SRS) model [29], the ideal cluster fractions
$$x_j^0 = g_j\, x^{n_j}\, (1-x)^{n-n_j} \tag{4}$$
are employed, which arise from a purely stochastic distribution of the clusters. They are independent of the temperature and the clusters' excess energies; hence, this case can be interpreted as the high-temperature limit of the GQCA [24].
3. The microscopic decomposition model (MDM) assumes that the cations of type A (B) are more likely to occur close to cations of type A (B) [24]. This is realized by cluster fractions that interpolate linearly between the binary end components, i.e.
$$x_j^{\mathrm{MDM}} = \begin{cases} 1-x & \text{for } j=0, \\ x & \text{for } j=J, \\ 0 & \text{otherwise.} \end{cases} \tag{5}$$
Within the MDM, mixing does not lead to a gain in internal energy, which can be the case under certain preparation conditions. For positive excess energies, the MDM represents the low-temperature limit of the GQCA.

In this work, the results for the two isostructural rs and wz alloys are compared with those of the heterostructural one. Thereby, the index j accordingly runs to $J = 21$ (isostructural wz system), $J = 15$ (isostructural rs system) or $J = 37$ (heterostructural alloy) [24].

2.2. *Computational details*

The QP electronic structures as well as the input for computing the macroscopic DFs are calculated using the Vienna *ab initio* simulation package (VASP) [33–36]. Throughout, the Mg 2p and Mg 3s as well as the O 2s and O 2p electrons are treated as valence electrons. For Zn and Cd, the Zn 3d and Cd 4d states are included as valence states, respectively, together with the Zn 4s and Cd 5s electrons. In order to obtain converged results for the pseudobinary alloys, a plane-wave cutoff energy of 450 eV is chosen. Moreover, the projector-augmented

wave (PAW) method is applied to describe the wave functions in the core regions [37–39]. The optical transition-matrix elements that are necessary to compute the DFs are calculated in the longitudinal approximation [36].

2.3. *Quasiparticle* (*QP*) *electronic structure*

A description of the QP electronic structure of the macroscopic alloys by means of the cluster expansion method requires the respective QP electronic structure of all different clusters that occur in the expansion. Currently, Hedin's GW approximation [40], $\Sigma = \mathrm{i}\hbar GW$, is the state-of-the-art approach for calculating the electronic self-energy Σ. Thereby, W is the dynamically screened Coulomb potential and G denotes the single-particle Green's function [41, 42]. Solving the QP equation including Σ leads to an electronic structure that accounts for the reaction of the electrons to the single-particle excitation that occurs e.g. in photoemission experiments. Thus, the resulting electronic states can be compared to the measured photoemission spectra or band structures from angle-resolved photoemission spectroscopy.

Usually, QP energies are obtained by correcting an initial electronic structure from the solution of the Kohn–Sham equation [43] within density-functional theory [44] (DFT) by means of first-order perturbation theory [45]; this approach is denoted by G_0W_0 and requires an initial electronic structure not too far from the final results. For the oxides studied in this work, DFT based on a generalized-gradient approximation (GGA) to exchange and correlation drastically underestimates the fundamental band gaps, the valence-band (VB) widths and the binding energies of the d bands [23]. Therefore, a better starting point for the initial electronic structure is crucial. It has been shown for several oxides that the HSE03 hybrid functional [46, 47] provides an excellent starting point for the G_0W_0 calculation, since the values for the fundamental band gaps as well as the d-band binding energies are reasonably close to experimental findings [7, 48–53].

In this work, Γ-centered $3 \times 3 \times 3$ Monkhorst–Pack [54] (MP) **k**-point meshes along with at least 1100 conduction bands (CBs) have been used to carry out the HSE03 + G_0W_0 calculations, which yield QP energies converged to within 0.1 eV. These results have been used for the calculation of the DOSs that are discussed (including a Gaussian broadening of 0.1 eV) in sections 3.5 and 3.6. With respect to previous calculations [7, 48, 49], the shape of the all-electron charge density is more accurately reproduced on the plane-wave grid in this work, because higher moments have been taken into account within the PAW implementation of the GW scheme [35, 55]. While this does not influence the HSE03 results, it has an impact on the G_0W_0 calculations, since they lack (for computational reasons) an exact implementation of the one-center terms [35, 56]. As a consequence, the fundamental band gap of wz-ZnO is about 0.29 eV smaller than discussed earlier [7, 48, 49]. For rs-MgO and rs-CdO, the influence has been found to be not larger than 0.1 eV. Even though this method slightly underestimates the fundamental gaps, it is well suited to the description of the QP electronic structure of the alloys as well as the trends with varying composition or preparation conditions.

For bulk MgO, ZnO and CdO, the influence of the spin–orbit interaction has also been calculated [7, 48], even taking strain [57] as well as non-equilibrium crystal structures [49] into account. It has been found that the spin–orbit coupling (SOC) only slightly modifies the Kohn–Sham states and, hence, the impact on the screened Coulomb potential W is expected to be small. Therefore, it is well justified to neglect the influence of the spin–orbit interaction on the QP *corrections* in order to obtain QP energies that account for the SOC-related effects.

Consequently, QP energies including SOC are obtained by adding QP shifts calculated without SOC to HSE03 eigenvalues that include spin–orbit interaction effects [39, 49, 57]. This approach, inspired by perturbation theory, is expected to produce reasonable results, especially because the absolute spin–orbit-induced shifts are small compared with the QP corrections for the materials studied in this work. It is employed to calculate the QP energies described in sections 3.1–3.4.

2.4. Dielectric function (DF): excitonic and local-field effects

In order to describe the optical absorption properties of the alloys, their frequency-dependent macroscopic DF is studied as the central quantity. It has been shown before that for its accurate description, the attractive electron–hole interaction is significant in MgO, ZnO and CdO [7, 48]. In addition, it is essential to take LFEs into account for the calculation of the macroscopic DFs. Both are achieved by solving [58, 59] the Bethe–Salpeter equation (BSE) for the optical polarization function [42, 60, 61]. For the actual solution of the integral BSE, it is typically transformed into an eigenvalue problem for the excitonic electron–hole pair Hamiltonian [62–64],

$$\hat{H}(cv\mathbf{k}, c'v'\mathbf{k}') = \left[\varepsilon_c^{\mathrm{QP}}(\mathbf{k}) - \varepsilon_v^{\mathrm{QP}}(\mathbf{k})\right]\delta_{cc'}\delta_{vv'}\delta_{\mathbf{k}\mathbf{k}'} - W(cv\mathbf{k}, c'v'\mathbf{k}') + 2\bar{v}(cv\mathbf{k}, c'v'\mathbf{k}'). \tag{6}$$

In equation (6), the first summand on the main diagonal represents the excitation of non-interacting quasielectron–quasihole pairs with excitation energies that are determined as the difference in the QP energies $\varepsilon^{\mathrm{QP}}$ of the CB (c) and VB (v) states at each $\mathbf{k}$ point of the Brillouin zone (BZ). Their interaction is described by the second and third terms, which contain the statically screened Coulomb attraction of the electron and the hole, $-W$, as well as the unscreened electron–hole exchange, $2\bar{v}$, to account for the optical LFEs [42, 65].

To calculate converged results for optical spectra, two partially competing requirements have to be fulfilled: while the investigation into high-energy optical transitions necessarily demands the inclusion of a large number of CBs, a thorough description of the low-energy optical transitions requires a fine $\mathbf{k}$-point sampling of the BZ to converge Wannier–Mott-like bound excitonic states and, hence, the spectral shape of the absorption onset [66]. Both requirements independently lead to very high computational costs, not only for the calculation of the starting electronic structure but also for that of the excitonic Hamiltonian itself. This will be addressed in the following.

The method introduced in section 2.3 has successfully been applied to calculate the QP electronic structure of MgO, ZnO and CdO [7, 48–52]. However, due to the extremely high computational cost of the HSE03 + G_0W_0 approach, a problem arises when many more $\mathbf{k}$ points or bands have to be taken into account. In particular, computing the matrix elements in the BSE Hamiltonian, equation (6), by means of the HSE03 + G_0W_0 method would impose impossibly high demands on memory and processor power [47]. To circumvent this problem, the HSE03 + G_0W_0 eigenvalues and wave functions are mimicked by those of a GGA + U approach with an additional scissors shift Δ [7, 48, 58, 59]. Here, the GGA + U scheme of Dudarev *et al* [67] is applied together with the PW91 GGA parametrization of Perdew and Wang [68, 69]. The scissors operator [41] Δ approximately describes the QP effects by rigidly shifting all CBs. In this work, the two parameters U and Δ are fixed based on a comparison with the HSE03 + G_0W_0 results: while U is adjusted in such a way that the energetic position of the d bands obtained from the GGA + U calculation matches the HSE03 + G_0W_0 one,

Δ is used to enlarge the fundamental gap until it is identical to the HSE03 + G_0W_0 value for each cluster. It has been shown before that $U = 6.5$ eV ($U = 4.5$ eV) fulfills this requirement for the Zn 3d (Cd 4d) electrons [7]. Moreover, the calculation of W in equation (6) requires a reasonable approximation for the screening in the system. Instead of using merely a static dielectric constant, a model function [70, 71] is employed, which requires the electronic static dielectric constant ε_∞ as the input parameter. In this work, the value calculated within the random-phase approximation (RPA), i.e. based on each individual cluster's GGA + U electronic structure, is used.

In this work, two different **k**-point meshes are employed to sample the BZ when computing the DFs: optical transitions with excitation energies below 5.8 eV (within GGA + U) are studied using a $9 \times 9 \times 9$ MP **k**-point mesh; all higher excitations are calculated using a $4 \times 4 \times 4$ mesh. In both cases, the **k** points are shifted by a small random vector. This shift of the entire **k** grid lifts symmetry degeneracies inherently present in MP **k**-point sets and therefore improves the convergence of the respective optical quantities [7].

Despite this strategy, very large matrices with ranks of up to 230 000 are obtained for the alloys, which equal several 10 to several 100 gigabytes worth of memory and hard-disk space. Fortunately, the prohibitively expensive direct diagonalization of these matrices can be bypassed by transforming the calculation of the DF into an initial-value problem that is treated using an efficient time-evolution scheme [65, 72]. This approach scales quadratically with the rank of the excitonic Hamiltonian and therefore allows the treatment of such large matrices. To account for broadening mechanisms that are relevant in the experiment, e.g. those due to finite lifetimes or temperatures, a Lorentzian broadening of 0.1 eV is applied to the calculated DFs.

3. Electronic structure

In the following, the cluster expansion method as presented in section 2.1 is used to compute the band structures and DOSs of the alloys based on the respective quantities calculated within the HSE03(+SOC) + G_0W_0 approach (cf section 2.3) for all individual clusters. Thus, it is important to study the QP energies of different clusters on a *common* absolute energy scale. In order to align the QP energies of the individual clusters, the branch-point energy [73–77] (BPE) is considered as the universal level of reference. At the branch point, the bands change their character from predominantly acceptor-like (usually VB states) to donor-like (usually CB states). It is assumed that the global Fermi level is pinned at the BPE, which leads to an energetic alignment of the cluster configurations in the alloys. Here, the BPEs are calculated for each cluster (cf table 1) using a modified Tersoff approach [77]. Since 16-atom supercells are studied in this work, the number of bands involved in the averaging procedure (equation (1) in [77]) was adjusted accordingly, leading to a total of eight CBs and 16 VBs for both the wz and the rs crystal structures.

3.1. QP energies: isostructural wurtzite (wz) alloys

The difficulty of defining a band structure for pseudobinary alloys arises from a broken translational symmetry in these systems [25]. In the following, this is illustrated for the $Mg_xZn_{1-x}O$ and $Cd_xZn_{1-x}O$ alloys. The QP energies (including SOC) of the lowest CB and the uppermost three VBs at the Γ point of the BZ have been calculated and aligned using the BPE (see table 1) for each cluster. For the bulk crystals in the wz structure, which represent the binary end components of the alloys, these states are classified as Γ_5 and Γ_1 (without SOC)

Table 1. Fundamental band gaps $E_{g,j}$ (in eV) of the individual clusters $X_{n_j}Zn_{8-n_j}O_8$ (X = Mg, Cd) of the cluster expansion of $X_xZn_{1-x}O$ alloys calculated using the HSE03 + SOC + G_0W_0 method. In addition, the branch-point energies $E_{BPE,j}$ (in eV) are given with respect to the VBM. The cluster class j and the number n_j of cations of type X are indicated (cf [24]).

j	n_j	$E_{g,j}$	$E_{BPE,j}$	j	n_j	$E_{g,j}$	$E_{BPE,j}$	j	n_j	$E_{g,j}$	$E_{BPE,j}$	j	n_j	$E_{g,j}$	$E_{BPE,j}$
wz-$Mg_{n_j}Zn_{8-n_j}O_8$															
0	0	2.92	3.27	6	3	4.10	3.83	12	4	4.55	4.10	18	6	5.29	4.34
1	1	3.29	3.45	7	3	3.97	3.70	13	4	4.43	3.95	19	6	5.17	4.23
2	2	3.59	3.56	8	4	4.21	3.78	14	5	4.75	4.04	20	7	5.77	4.57
3	2	3.64	3.59	9	4	4.34	3.87	15	5	4.91	4.20	21	8	6.19	4.73
4	2	3.76	3.69	10	4	4.39	3.92	16	5	4.71	4.03				
5	3	3.93	3.69	11	4	4.28	3.80	17	6	5.39	4.43				
j	n_j	$E_{g,j}$	$E_{BPE,j}$	j	n_j	$E_{g,j}$	$E_{BPE,j}$	j	n_j	$E_{g,j}$	$E_{BPE,j}$	j	n_j	$E_{g,j}$	$E_{BPE,j}$
rs-$Mg_{n_j}Zn_{8-n_j}O_8$															
0	0	2.88	3.33	4	3	3.94	3.65	8	4	4.20	3.77	12	6	6.02	4.84
1	1	3.15	3.41	5	3	3.73	3.63	9	4	3.98	3.76	13	6	4.87	4.07
2	2	3.50	3.52	6	4	5.03	4.33	10	5	5.49	4.58	14	7	6.61	5.07
3	2	3.34	3.52	7	4	5.07	4.38	11	5	4.51	3.91	15	8	7.49	5.43
j	n_j	$E_{g,j}$	$E_{BPE,j}$	j	n_j	$E_{g,j}$	$E_{BPE,j}$	j	n_j	$E_{g,j}$	$E_{BPE,j}$	j	n_j	$E_{g,j}$	$E_{BPE,j}$
wz-$Cd_{n_j}Zn_{8-n_j}O_8$															
0	0	2.92	3.27	6	3	1.92	2.80	12	4	1.66	2.67	18	6	1.28	2.50
1	1	2.53	3.10	7	3	1.93	2.81	13	4	1.69	2.69	19	6	1.24	2.46
2	2	2.17	2.90	8	4	1.56	2.59	14	5	1.47	2.58	20	7	1.10	2.41
3	2	2.24	2.97	9	4	1.69	2.71	15	5	1.45	2.57	21	8	0.96	2.33
4	2	2.23	2.95	10	4	1.65	2.67	16	5	1.42	2.54				
5	3	1.86	2.75	11	4	1.68	2.68	17	6	1.26	2.48				
j	n_j	$E_{g,j}$	$E_{BPE,j}$	j	n_j	$E_{g,j}$	$E_{BPE,j}$	j	n_j	$E_{g,j}$	$E_{BPE,j}$	j	n_j	$E_{g,j}$	$E_{BPE,j}$
rs-$Cd_{n_j}Zn_{8-n_j}O_8$															
0	0	2.88	3.33	4	3	1.61	2.73	8	4	1.01	2.32	12	6	0.91	2.36
1	1	2.04	2.78	5	3	1.10	2.27	9	4	0.96	2.32	13	6	1.00	2.42
2	2	1.78	2.73	6	4	1.49	2.75	10	5	0.95	2.37	14	7	0.78	2.43
3	2	1.22	2.23	7	4	1.47	2.73	11	5	0.90	2.34	15	8	0.75	2.48

or Γ_{7-}, Γ_{7+} and Γ_9 (with SOC), respectively [49, 57, 78]. The energetic splittings between these states are due to the crystal field or the spin–orbit interaction. However, such a symmetry classification is no longer possible for the clusters that contain two *different* types of cations, since, due to the reduced symmetry, these definitions do not hold anymore. Even in the absence of SOC, all three states at the top of the VBs are non-degenerate for intermediate compositions x. Hence, a clear assignment to the crystal-field splitting and the SOC-induced splitting is not feasible because interpreting the band structures of alloys in terms that only exist for the binary end components is impossible.

In addition, it is not straightforward to relate the energy states that occur in *different* 16-atom cluster cells. Hence, they are simply grouped according to their energetic ordering. However, information about possible crossings cannot be obtained, as will be discussed below.

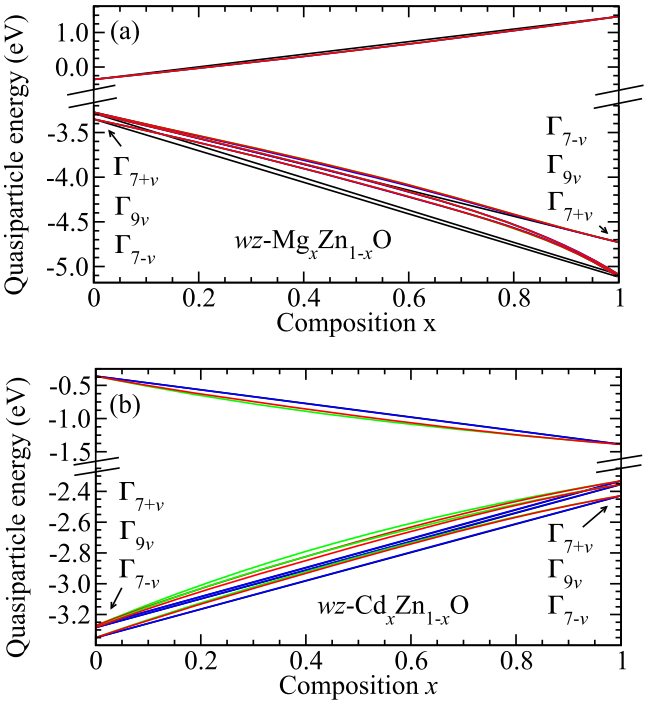

Figure 1. QP energies (including SOC) of the uppermost three VB states and the lowest CB state at the Γ point for wz-$Mg_xZn_{1-x}O$ (a) and wz-$Cd_xZn_{1-x}O$ (b) alloys versus composition x. The BPE has been used as zero energy. Cluster fractions from the GQCA for $T = 300\,\mathrm{K}$ (blue curves) and $T = 1100\,\mathrm{K}$ (red curves) have been used. The solid green lines are obtained using the ideal cluster fractions and the black curves, representing the result from the MDM, are included for comparison. For the binary end components, the band ordering is indicated.

Instead of generalizing the picture of the alloys' band structure [25], equation (1) is used together with the different cluster fractions to calculate the configurational averages for the QP energies at Γ within the GQCA, the SRS model and the MDM as a function of x and T.

For wz-$Mg_xZn_{1-x}O$ the plot in figure 1(a) indicates that the GQCA results for $T = 300\,\mathrm{K}$ and $T = 1100\,\mathrm{K}$ largely agree with each other and with the SRS curves. However, the MDM results deviate from the other cases, which indicates a significant difference between a linear interpolation of the energy levels of the binary end components and the results from averages that take all clusters into account to simulate a random alloy. Figure 1(a) clearly shows that the MDM predicts larger splittings of the uppermost two VB states for intermediate values of $x \approx 0.2, \ldots, 0.6$. Both the SRS model and the GQCA agree in finding an increase in the splitting between these two levels only when $x > 0.7$, which is accompanied by a remarkable bowing.

In the case of the isostructural wz-$Cd_xZn_{1-x}O$ alloy, the MDM curves and the curves obtained using GQCA for $T = 300\,\mathrm{K}$ show good agreement (cf figure 1(b)), whereas the GQCA curve for $T = 1100\,\mathrm{K}$ is much closer to the SRS result. While the VB splittings are smaller than those for $Mg_xZn_{1-x}O$, it can be clearly seen that the influence of the alloy statistics on the CB edge is stronger for $Cd_xZn_{1-x}O$.

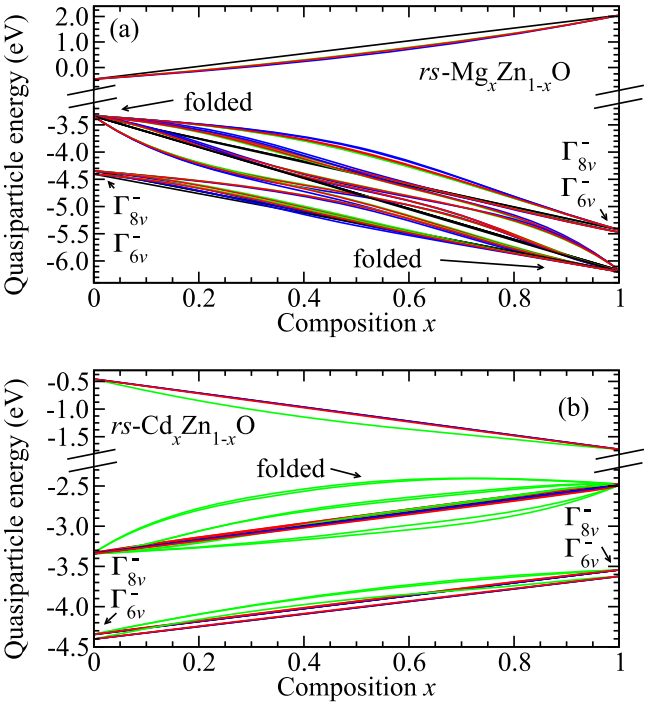

Figure 2. QP energies (including SOC) of the uppermost three VB and the lowest CB state at the Γ point for rs-$Mg_xZn_{1-x}O$ (a) and rs-$Cd_xZn_{1-x}O$ (b) alloys versus composition x. The BPE has been used as zero energy. Cluster fractions from GQCA for $T = 300\,\mathrm{K}$ (blue curves) and $T = 1100\,\mathrm{K}$ (red curves) have been used. The solid green lines are obtained using the ideal cluster fractions and, in comparison, the black curves show the results from the MDM. For the binary end components, the band ordering is indicated.

For the structural parameters of wz-$Mg_xZn_{1-x}O$ and wz-$Cd_xZn_{1-x}O$ alloys, the same trends for the agreement between the predictions of the different models that describe the cluster fractions have been observed before. This was explained using the respective excess energies [24].

3.2. QP energies: isostructural rock salt (rs) alloys

For the isostructural rs-$Mg_xZn_{1-x}O$ and rs-$Cd_xZn_{1-x}O$ alloys, the configurational averages of the QP energies at Γ for the upper VB region (formed by a fourfold degenerate Γ^-_{8v} and a twofold degenerate Γ^-_{6v} state [79] in the case of the binary end components) and the lowest CB are presented in figure 2. In the band structure of *pure* rs-CdO (as well as pure rs-ZnO) it has been observed that due to the *pd* repulsion, the fundamental band gap is *indirect* and occurs between the VB maximum (VBM) at L and the CBM at Γ [7, 23]. Since the 16-atom cluster cells are larger than the primitive unit cells of an rs crystal (two atoms), the corresponding band structures of the cluster cells contain *folded* states, e.g. the uppermost states at L in the fcc BZ are folded onto the Γ point of the cluster BZ. In general, it is not possible to distinguish between states that occur also at the Γ point in the BZ of the two-atom rs cell and states that are merely folded into the smaller BZ of the alloy. The problems that arise from the folding are indicated in figure 2.

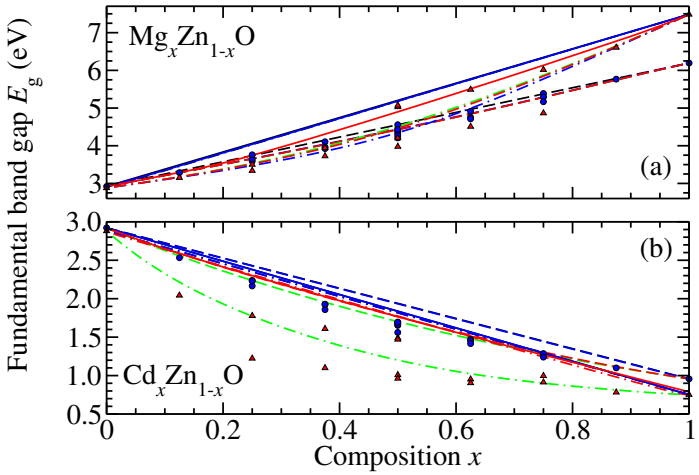

Figure 3. Difference in the QP energies of the uppermost VB and the lowest CB state for $Mg_xZn_{1-x}O$ (a) and $Cd_xZn_{1-x}O$ (b) alloys versus composition x. The curves are obtained using wz clusters only (dashed lines), rs clusters only (dash-dotted lines) or both types of cluster (solid lines). Cluster fractions from the GQCA for $T = 300$ K (blue curves) and $T = 1100$ K (red curves) as well as ideal cluster fractions (green curves) are used. For comparison, the black curves show the result from the MDM. The fundamental gaps of the individual rs (red triangles) and wz (blue circles) clusters are also included.

At least for rs-$Cd_xZn_{1-x}O$, the folded bands lie at the top of the VBs and are energetically well separated from the regular states at Γ for all clusters since the *pd* repulsion occurs in both rs-ZnO and rs-CdO away from the Γ point (cf figure 2(b)). Consequently, the VB top of rs-$Cd_xZn_{1-x}O$ alloys is formed by these L_{3v}-derived states. However, in the case of the rs-$Mg_xZn_{1-x}O$ alloy, this strict separation does not occur since pure rs-MgO has a direct gap due to the lack of *pd* hybridization. Thus, as clearly pointed out by figure 2(a), the states in the alloy band structure cannot be properly assigned and mixing occurs for intermediate compositions. Due to the difficulties in the assignment of single states, the discussion of integral quantities, such as the DOSs or the DFs, is more meaningful for the alloys and will be done in sections 3.5, 3.6 and 4.

Nevertheless, the uppermost VBs of both alloy systems are governed by two effects: (i) two different groups of VBs emerge for the binary end components (cf figure 2). One group results from Γ_{8v}^- and Γ_{6v}^- states that occur at the Γ point in the fcc BZ and that are separated by the spin–orbit splitting. The other group is derived from the L_{3v}-related states. (ii) An important influence arises from the spin–orbit splitting, which increases from rs-MgO over rs-ZnO to rs-CdO [49]. Moreover, it is important to keep in mind that the SOC at Γ is much larger for the rs polymorphs than for the wz polymorphs due to the effects of *pd* hybridization [49].

3.3. Fundamental band gaps

Another quantity that is well defined for all clusters is the fundamental band gap, as the difference in the QP energies of the lowest CB state and the highest VB state. In figure 3, the configurational averages of the gap values are shown for isostructural as well as heterostructural

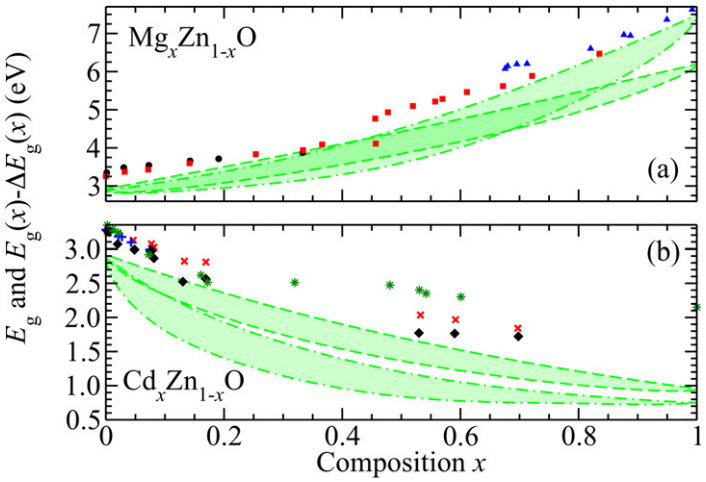

Figure 4. The shaded areas are limited by $E_g(x)$ (upper limit), and $E_g(x) - \Delta E_g(x)$ (lower limit), as calculated within the SRS model for isostructural $Mg_xZn_{1-x}O$ (a) and $Cd_xZn_{1-x}O$ (b) alloys. The curves are obtained using wz clusters (dashed lines) or rs clusters (dash-dotted lines) only. The calculated results are compared with experimental values from [80] (black circles), [81] (blue triangles) and [82] (red squares) in the case of $Mg_xZn_{1-x}O$ as well as those from [20] (blue '+' symbols), [18] (red '×' symbols represent the optical absorption and black diamonds the photoluminescence) and [21] (green '∗' symbols) in the case of $Cd_xZn_{1-x}O$.

$Mg_xZn_{1-x}O$ and $Cd_xZn_{1-x}O$ alloys together with the results obtained for the individual clusters (cf. table 1).

For wz-$Mg_xZn_{1-x}O$ again, good agreement between the results obtained within the GQCA and the SRS model is observed, whereas these curves differ slightly from the prediction of the MDM (cf figure 3(a)). Since, for $Mg_xZn_{1-x}O$, the gap values of the individual rs clusters cover a larger range than do those of the wz clusters, both the GQCA and the SRS curves deviate more from the MDM results in the rs case. The similarity of the direct gap of wz-ZnO to the indirect gap of rs-ZnO is the reason why the MDM curves of heterostructural $Mg_xZn_{1-x}O$ and those of rs-$Mg_xZn_{1-x}O$ are very close to each other. The GQCA for the heterostructural system predicts slightly smaller values.

The indirect gaps found for rs-ZnO as well as rs-CdO become the direct ones for the 16-atom clusters of $Cd_xZn_{1-x}O$ since the folded states are the uppermost ones for all rs clusters. Since the fundamental gaps observed for the wz crystal structure are similar to those for the rs case, the results for the two isostructural alloys are much closer to each other than in the case of $Mg_xZn_{1-x}O$. It can be seen from figure 3(b) that the SRS model leads to the largest deviations, while the bowing remains small for the other statistics, indicating dependence on the cluster statistics and, hence, on the sample preparation.

The configurational averages $E_g(x)$ of the gap given in figure 3 can be measured as an absorption edge for the alloys, provided that excitonic effects are negligible and the optical transitions are not dipole forbidden. However, the macroscopic alloy is formed by a distribution of clusters. Therefore, when compared to photoluminescence experiments, it has to be taken into account that the radiative electron–hole recombination happens locally for the *lowest*

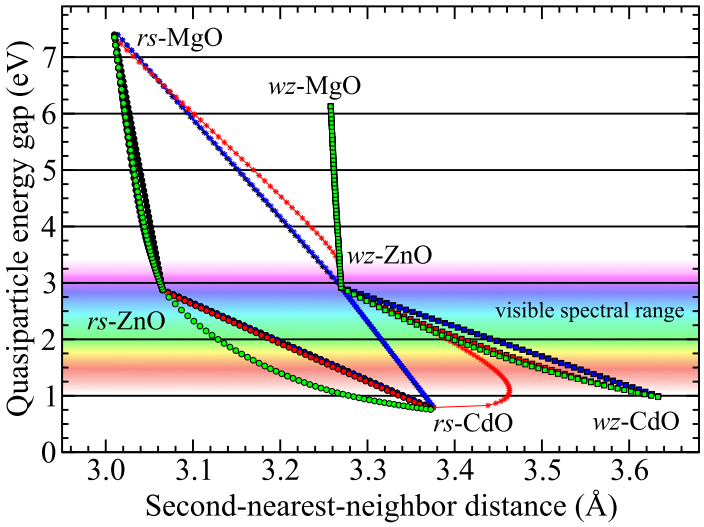

Figure 5. Fundamental band gap versus second-nearest-neighbor distance for isostructural wz (squares) and rs (dots) as well as heterostructural (stars) $Mg_xZn_{1-x}O$ and $Cd_xZn_{1-x}O$ alloys. Configurational averages are depicted as calculated from the MDM (black), from the SRS (green) and from the GQCA for $T = 300$ K (blue) and $T = 1100$ K (red). Each symbol represents a variation in the composition by $\Delta x = 0.02$. The visible spectral range is marked.

electron–hole-pair energies. Hence, in order to account for the presence of clusters with band gaps that are smaller than the configurational average, it is necessary to include a certain deviation. In this work, the respective mean-square deviation $\Delta E_g(x)$ (cf equation (2)) is considered to describe this effect. Therefore, in figure 4, the curves describing both $E_g(x)$ and $E_g(x) - \Delta E_g(x)$ as calculated within the SRS model for the isostructural alloys are used as borders of the shaded areas.

Ohtomo *et al* [80] reported an experimental gap of 4.1 eV for a Mg content of $x \approx 0.33$, which agrees well with the result for the isostructural alloy found in this work as well as with a value of 4.2 eV derived from DFT in the local-density approximation combined with scissors operators for the gaps of wz-MgO and wz-ZnO [83]. Experimental gaps of about 6 eV at $x \approx 0.67$ or 7 eV at $x \approx 0.9$, as reported by Fritsch *et al* [81], can be explained by the curves calculated for the heterostructural or the isostructural rs-$Mg_xZn_{1-x}O$ alloys derived in this work. In addition, the occurrence of two different slopes of the curves describing the gap versus the composition for the isostructural rs and wz alloys (cf figure 3(a)) agrees with the findings reported in [82]. When compared to experimental values for the composition-dependent gap reported for $Cd_xZn_{1-x}O$ in [18, 20, 21], it is observed that the present results tend to slightly underestimate the experimental ones. This is attributed to the underestimation of the gaps in the calculations already found for pure ZnO and CdO [7]. Moreover, the optical transitions from the VBM into the folded states are dipole forbidden, i.e. the fundamental band gap shown in figure 3(b) tends to be smaller than the optical band gap in the case of rs-$Cd_xZn_{1-x}O$.

3.4. Bowing of the fundamental band gap

In order to draw conclusions on the ranges in which the band gaps of the alloy systems can be tuned and what the corresponding effect on the crystal lattice is, the configurational averages for

the fundamental band gaps are combined with those of the lattice parameters reported in [24]. The second-nearest-neighbor distances are used for the plot in figure 5, since they represent a parameter that describes the atomic geometry independently of the lattice symmetry. For wz crystals, it coincides with the a lattice constant and for the rs structure it is equal to $a_0/\sqrt{2}$, where a_0 denotes the cubic lattice constant.

From figure 5, it becomes clear that (depending on the preparation conditions) the variation of the second-nearest-neighbor distance can amount to 0.1 Å within the same alloy system for a fixed value of the gap (see e.g. rs-$Cd_xZn_{1-x}O$ and $E_g \approx 1.5$ eV). However, in most cases, this variation is smaller. Moreover, the plot impressively shows that significant deviations from the linear variation of the fundamental band gap with the second-nearest-neighbor distance can occur for the GQCA as well as the SRS model, because the preparation conditions sensitively affect both the band gaps and the lattice geometries. Consequently, also the bowing of the band gap has to be taken into account when tuning these properties in experiment.

Such a bowing of the fundamental band gap, i.e. the deviation from a linear variation of the gap E_g with the composition x, is typically quantified using the bowing parameter b. It is defined by the expression

$$E_g(x) = (1-x)\,E_g(A) + x\,E_g(B) - b\,x\,(1-x) \tag{7}$$

for the gap, in which $A = ZnO$ and $B = \{MgO, CdO\}$ in the respective crystal structures. For isostructural wz-$Mg_xZn_{1-x}O$, small values for b of 0.48 eV (SRS as well as GQCA for $T = 1100$ K) and 0.44 eV (GQCA for $T = 300$ K) are obtained, which agree well with the values of 0.56 eV [83] and 0.87 eV [84] from other calculations. With values of 2.58 eV (SRS), 3.12 eV (GQCA, $T = 300$ K) or 2.74 eV (GQCA, $T = 1100$ K) the bowing is larger for rs-$Mg_xZn_{1-x}O$, in rough agreement with another calculated result of 3.1 eV [85]. Moreover, in the present work, it is found that the values for the heterostructural $Mg_xZn_{1-x}O$ alloy are strongly temperature- and, hence, preparation-dependent, as they vary from 0.07 eV ($T = 300$ K) to 1.30 eV ($T = 1100$ K). Photocurrent measurements of $Mg_xZn_{1-x}O$ layers with $x < 0.3$ indicate a rather linear behavior of the absorption edge [86]. Disagreement with the results for b obtained in another calculation [87] is found, which arises from the use of a least-squares fit in the present work as opposed to the use of an approximation based on only three data points in [87].

For both crystal structures of $Cd_xZn_{1-x}O$, the bowings obtained within GQCA for room temperature are smaller than 0.023 eV, whereas the results for $T = 1100$ K are 0.72 eV (wz-$Cd_xZn_{1-x}O$), 0.18 eV (rs-$Cd_xZn_{1-x}O$) or 0.29 eV for the heterostructural alloy. The SRS model yields even larger values of 0.95 eV (wz-$Cd_xZn_{1-x}O$) or 2.51 eV (rs-$Cd_xZn_{1-x}O$). Consequently, there is a nonlinear composition dependence of the fundamental gaps for most preparation conditions. Unfortunately, no measured values for the bowing in $Cd_xZn_{1-x}O$ alloys could be found in the literature. Comparison to a value of $b = 1.9$ eV derived by Fan *et al* [84] from the gaps of individual clusters reveals good agreement. Moreover, as recently found also for InGaN [88], the curves in figure 3 indicate that a composition-independent bowing parameter might not be enough to capture the behavior of the band gap over the entire composition range.

Moreover, figure 4 shows that the bowings of $E_g(x) - \Delta E_g(x)$ (as calculated within the SRS model) are larger than those of $E_g(x)$. In the case of wz-$Mg_xZn_{1-x}O$ (rs-$Mg_xZn_{1-x}O$), the respective bowing amounts to 2.84 eV (6.14 eV). For wz-$Cd_xZn_{1-x}O$ (rs-$Cd_xZn_{1-x}O$), a value of $b = 2.33$ eV ($b = 4.00$ eV) is derived for $E_g(x) - \Delta E_g(x)$.

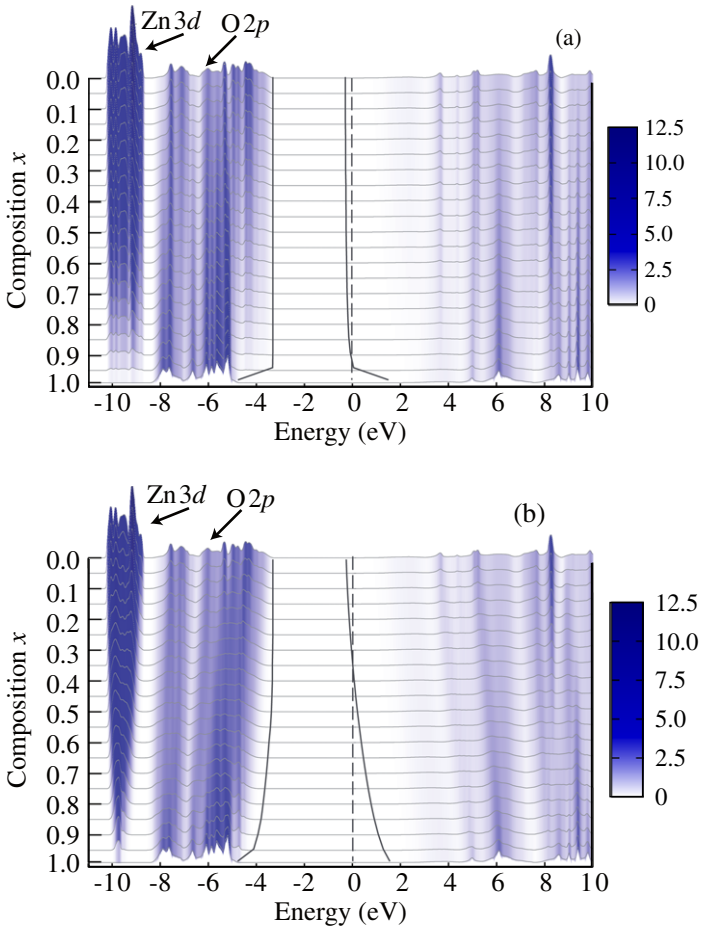

Figure 6. Plot of DOS in $(\text{eV} \cdot \text{pair})^{-1}$ (gray lines) of the isostructural wz-$Mg_xZn_{1-x}O$ alloy versus composition x. The BPE has been used as zero energy (black dashed line). The curves are calculated using the cluster fractions from the MDM (a) or the SRS model (b). As a guide to the eye, the black solid lines indicate where the DOS in the gap region decreases to 0.01 $(\text{eV} \cdot \text{pair})^{-1}$.

3.5. Densities of states (DOSs): isostructural wz-$Mg_xZn_{1-x}O$

The configurational average for the DOS of the alloys is obtained as a point-by-point average of the BPE-aligned QP DOS (without SOC) of the individual clusters according to equation (1). Since integrating the DOS yields the total number of states, i.e. a number that is additive, no sum rules are violated when this procedure is applied [89].

In order to clarify the impact of the different cluster statistics, the results for the DOS of the isostructural wz-$Mg_xZn_{1-x}O$ alloy obtained within the MDM are compared to those from the SRS model in figure 6 (the GQCA results strongly resemble those of the SRS model). As expected for the MDM, figure 6(a) shows that the DOS curves of pure wz-ZnO linearly transform into those of the pure wz-MgO as x increases. Consequently, the energy positions and widths of all structures or peaks remain constant and only the respective heights depend on x (see, for example, the Zn 3d-related structure in figure 6(a)). In contrast, the SRS

model, in which all clusters contribute, also reproduces the changes of peak widths or peak positions (relative to the BPE) that can occur with varying composition x (cf figure 6(b)). Correspondingly, even though the peak caused by the Zn 3d electrons vanishes for both statistics, figure 6 shows that the SRS yields a narrowing of the respective bandwidth since more clusters with less Zn atoms contribute to the average with increasing the content of Mg in the alloy. For that reason, also the peak shape is influenced.

Figure 6 includes lines that indicate where the DOS becomes smaller than 0.01 $(\text{eV} \cdot \text{pair})^{-1}$ as an indication of the behavior of the VBM and the CBM. Due to the strongly dispersive lowest CB, which appears in all oxides [7, 49], it is difficult to define the lowest-energy conduction states. In addition, these lines point out that at intermediate compositions x, the fraction of clusters that have fundamental band gaps close to those of wz-ZnO is not negligible for both statistics and leads to a finite DOS. While the corresponding CB DOS is very low already for the bulk materials, this effect is more pronounced for the alloys.

The two series of spectra in figures 5(a) and (b) display another interesting fact. Independent of the preparation conditions and, hence, the microscopic distribution of MgO and ZnO bonds, the BPE lies in the CB for $x < 0.35$. Consequently, the wz-$Mg_xZn_{1-x}O$ alloys are likely to show an n-type behavior [77].

3.6. DOSs: heterostructural $Mg_xZn_{1-x}O$ and $Cd_xZn_{1-x}O$

It was shown recently that the MDM and the GQCA for room temperature predict similar structural [24] and electronic properties (see above) for the heterostructural $Mg_xZn_{1-x}O$ or $Cd_xZn_{1-x}O$ alloys, respectively. Hence, comparison of the DOS for both cases in the respective material system shows that the GQCA results for room temperature strongly resemble those of the MDM. Since, as discussed above, the MDM DOS is merely a linear transition between the DOSs of the binary end components, in figure 7, the configurational average calculated within the GQCA for $T = 1100\,\text{K}$ is shown instead. In this case, the GQCA predicts that more than 50% of the clusters will occur in the wz crystal structure also above $x = 0.5$ (cf [24]).

Interestingly, figure 7 shows that the peaks related to the Zn 3d electrons evolve into an O 2p-derived complex for $Mg_xZn_{1-x}O$. Above $x \approx 0.7$, a structure related to these O 2p electrons emerges within the Zn 3d states (cf figure 7(a)), since the energy position of the VBM with respect to the BPE simultaneously decreases with increasing x. Both the increase in the fundamental gap and the decrease in pd repulsion with increasing Mg content in the alloy lead to this decrease in the energy position of the O 2p-derived VB complex with respect to the BPE.

For $Cd_xZn_{1-x}O$, figure 7(b) clearly shows how the position of the d-derived states decreases in energy since the Cd 4d electrons are bound together stronger than are the Zn 3d electrons. In addition to that, the O 2p complex appears at higher energies with increasing x.

4. Optical properties

The optical properties of the alloys, including excitonic and LFEs, are studied by calculating the imaginary part of the DF for all respective clusters of the expansion. Since, in particular, the $Mg_xZn_{1-x}O$ alloys rests to be well investigated experimentally, the focus for the heterostructural alloys rests on this material system in this paper. As described above for the DOS, the configurational average for the imaginary part of the DF (averaged over all polarization

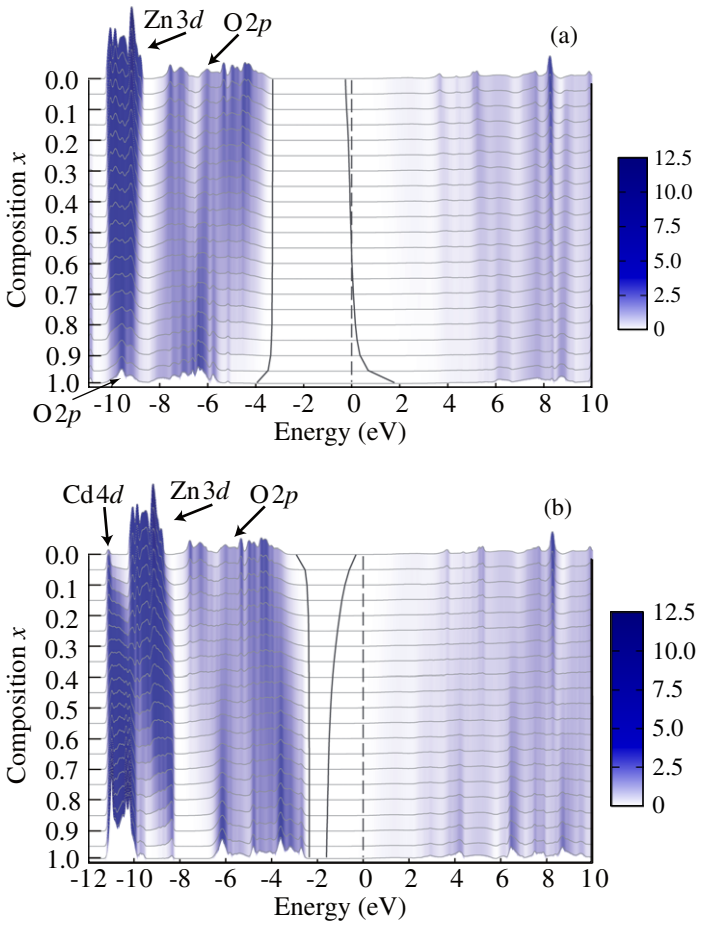

Figure 7. DOS in $(\mathrm{eV} \cdot \mathrm{pair})^{-1}$ (gray lines) of the heterostructural $Mg_xZn_{1-x}O$ (a) and $Cd_xZn_{1-x}O$ (b) alloys versus composition x, as obtained within the GQCA for $T = 1100\,\mathrm{K}$. The BPE has been used as zero energy (black dashed line). To guide the eye, the solid black lines indicate where the DOS in the gap region decreases to $0.01\ (\mathrm{eV} \cdot \mathrm{pair})^{-1}$.

directions) is performed at each energy individually using equation (1) along with the different cluster fractions. Since the squares of the plasma frequencies as well as the dielectric constants of the clusters are additive, the oscillator-strength sum rule as well as the screening sum rule are not violated by this procedure [89].

The DFs of the individual clusters are calculated using a supercell approach. Thereby, confinement effects due to real clustering, i.e. when an alloy with a smaller average gap is embedded in an alloy with a wider one, are neglected. They might reduce the electron–hole distance in a real sample and therefore increase exciton binding energies. As discussed for photoluminiscence above, it is expected that the electron–hole pair preferably recombines in an area in a real sample with the locally smallest gap. Thus, this area would contribute more strongly to the spectra, leading to the occurrence of pronounced excitonic peaks also in the alloys. Moreover, excitons bound to defects may occur for compositions close to the binary end components, i.e. for very small or very large compositions x.

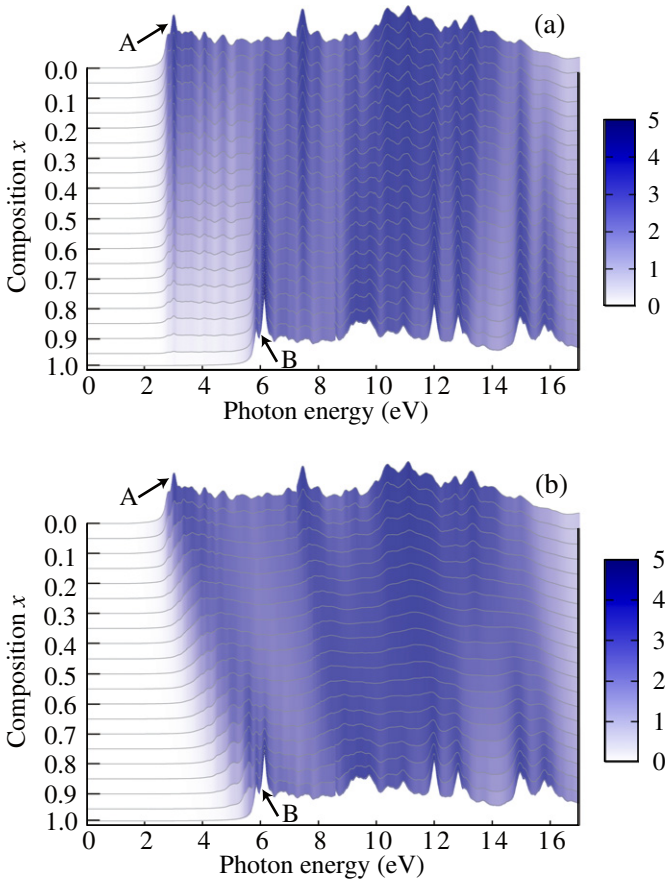

Figure 8. Imaginary part of the DF of wz-$Mg_xZn_{1-x}O$ versus composition x calculated using the MDM (a) and the SRS model (b). A (B) labels the excitonic bound state at the absorption edge of wz-ZnO (wz-MgO).

4.1. DF: isostructural wz-$Mg_xZn_{1-x}O$ and wz-$Cd_xZn_{1-x}O$

To emphasize the qualitative difference between the results from two limiting cluster statistics, the DF of wz-$Mg_xZn_{1-x}O$ obtained by means of the MDM is compared to the results of the SRS model in figure 8. At the onset of the DF of the pure compounds, peaks occur that are associated with a bound excitonic state at the absorption edge [7, 66] of either wz-ZnO or wz-MgO and are denoted by A or B, respectively. As already shown for the DOS (cf section 3.5), the MDM corresponds to a linear transition of the curve for wz-ZnO to the curve for wz-MgO as the value of x increases. Consequently, *both* excitonic peaks (A and B) occur for intermediate values of x in figure 8(a).

Comparison of the MDM result for the evolution of peaks A and B with increasing x to the one within the SRS model (cf figure 8(b)) reveals the strong dependence on cluster statistics. When the DFs of all clusters are taken into account for the configurational average, peaks A and B only occur in the x range close to the binary end components. For intermediate compositions, a very broad structure dominates the absorption edge. While this is in clear contrast to what was observed in figure 8(a), such a behavior has been reported in a spectral study of the photocurrents for wz-$Mg_xZn_{1-x}O$ for various x [86]. This indicates that the deposited

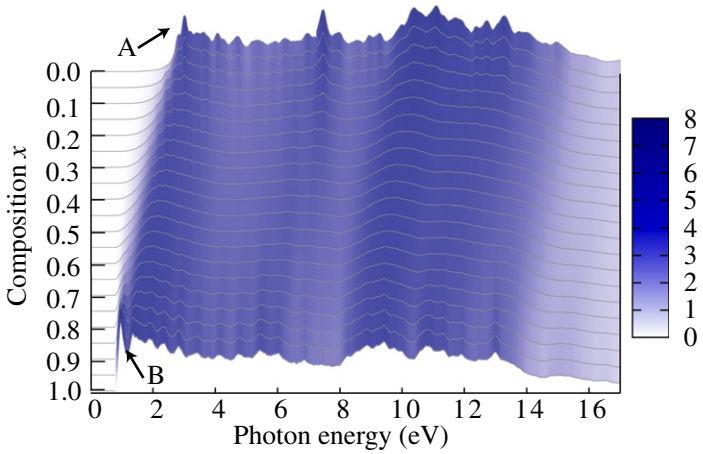

Figure 9. Imaginary part of the DF of wz-$Cd_xZn_{1-x}O$ versus composition x calculated using the SRS model. A (B) labels the excitonic bound state at the absorption edge of wz-ZnO (wz-CdO).

wz-$Mg_xZn_{1-x}O$ layers [86] possess a microstructure close to the one of a random alloy, since there is no clear indication of a clustering of pure MgO and ZnO, which would lead to spectra with the line shape given in figure 8(a). However, such a line shape caused by excitonic effects was found for the peak at the absorption edge reported for thin films in [19].

The same trends are observed for wz-$Cd_xZn_{1-x}O$. As discussed in section 3.6, for this alloy, the MDM results are close to those of the GQCA for $T = 300\,\mathrm{K}$ and the SRS results are similar to the GQCA results for $T = 1100\,\mathrm{K}$. As can be seen in figure 9, a pronounced excitonic peak occurs also close to the absorption edge of wz-CdO (in contrast to rs-CdO [7]). However, since all clusters contribute to the configurational average within the SRS model, it is strongly broadened for intermediate compositions. Nevertheless, the result in figure 9 shows that for small compositions, the excitonic peak of ZnO should still be visible as it has been found in absorption measurements [20]. In any case, a strong dependence of the structure of the absorption edge on the cluster fractions is observed. Therefore, in experiment it should be evident if larger regions of the pure material occur on a microscopic length scale in a real sample.

Figures 8 and 9 also depict the evolution of the peak structures with the composition at higher photon energies. Again it is observed that the SRS model tends to yield broad structures instead of distinct peaks. The origin of these peaks has been discussed in detail for rs-MgO, wz-ZnO and rs-CdO in [7].

4.2. DF: heterostructural $Mg_xZn_{1-x}O$

In addition to the configurational averages for the DFs of the isostructural alloys, those for the heterostructural $Mg_xZn_{1-x}O$ alloys are also calculated, since this material system is important from an experimental perspective [15, 16, 19, 86]. In figure 10, the result obtained using the SRS is shown. In comparison with the DFs discussed for isostructural wz-$Mg_xZn_{1-x}O$, figure 10 shows a totally different behavior: excitonic peaks that arise from both the wz and the rs absorption edges are visible for each end component, because wz as well as rs clusters contribute to the configurational average. The corresponding peaks are denoted by A and A′ as

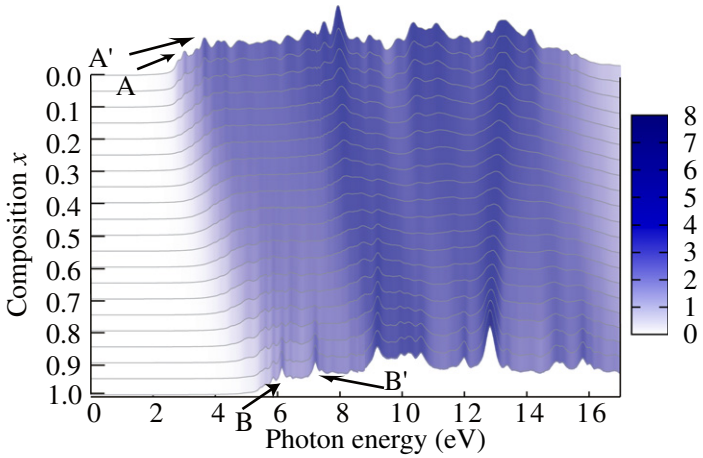

Figure 10. Imaginary part of the DF of heterostructural $Mg_xZn_{1-x}O$ versus composition x calculated using the SRS model. A (A′) labels the exciton bound state at the absorption edge of wz-ZnO (rs-ZnO), whereas B (B′) denotes that of wz-MgO (rs-MgO).

well as B and B′, respectively. For both binary limits, ZnO and MgO, the peak arising from the bound excitonic state of the wz polymorphs (A and B) occurs at lower photon energies than does that of the rs polymorphs (A′ and B′). This suggests that if significant amounts of both crystal structures occur in the macroscopic alloy, this should be clearly visible in the respective DF for alloy compositions close to the binary limits. However, as observed in the previous section, these peaks are significantly smeared out for intermediate compositions due to the configurational average for the SRS model.

5. Summary and conclusions

The electronic and optical properties of isostructural as well as heterostructural pseudobinary $Mg_xZn_{1-x}O$ and $Cd_xZn_{1-x}O$ alloys have been calculated using a combination of recent theoretical-spectroscopy techniques and a cluster expansion method. This approach has been applied to study the dependence of the fundamental band gap, the DOS or the DF on the composition of the alloys and to investigate the impact of the preparation conditions on these properties.

It has been shown that it is not feasible merely to interpret the splittings between the uppermost valence states in the QP band structure in terms of crystal-field splitting and spin–orbit-induced splitting. Configurational averages for the fundamental band gap of the alloys have been computed and used to derive the respective bowing parameters with varying composition, taking the preparation conditions into account. In agreement with experimental findings and other calculated results, remarkable bowings were found. Thus the effect is much stronger for $Mg_xZn_{1-x}O$ than it is for $Cd_xZn_{1-x}O$.

Moreover, configurational averages for spectral quantities, such as the DOSs of the isostructural and heterostructural alloys, as well as their DFs, were calculated. These results were used to investigate the behavior of the absorption edge and of high-energy peaks in the DOSs and the DFs with varying alloy composition or for different preparation conditions. The electron–hole interaction was taken into account for the calculation of the DFs, enabling

a study of the trends of the peaks related to bound excitonic states at the absorption edge. Since the occurrence of excitonic peaks in absorption spectra should be distinctly observable in experiments, these results can contribute to investigations of the composition of the alloys.

Acknowledgments

We thank S Haberhauer for fruitful discussions. The research presented here received funding from the European Community's Seventh Framework Programme (FP7/2007-2013) under grant agreement no. 211956 and from the Deutsche Forschungsgemeinschaft (project no. Be1346/20-1). A Schleife thanks the Carl-Zeiss-Stiftung for support. We acknowledge the grant of computer time from Höchstleistungsrechenzentrum Stuttgart and the HPC-EUROPA2 project (project no. 228398) with support from the European Commission–Capacities Area–Research Infrastructures.

References

[1] Ginley D S and Perkins J D 2010 Transparent conductors *Handbook of Transparent Conductors* ed D S Ginley (Berlin: Springer) 1–25
[2] Qin Y, Wang X and Wang Z L 2008 Microfibre–nanowire hybrid structure for energy scavenging *Nature* **451** 809–13
[3] Bae J, Song M K, Park Y J, Kim J M, Liu M and Wang Z L 2011 Fiber supercapacitors made of nanowire–fiber hybrid structures for wearable/flexible energy storage *Angew. Chem.* **123** 1721–5
[4] Comini E and Sberveglieri G 2010 Metal oxide nanowires as chemical sensors *Mater. Today* **13** 36–44
[5] Ohta H, Ichi Kawamura K, Orita M, Hirano M, Sarukura N and Hosono H 2000 Current injection emission from a transparent p–n junction composed of p-$SrCu_2O_2$/n-ZnO *Appl. Phys. Lett.* **77** 475–7
[6] Presley R E, Hong D, Chiang H Q, Hung C M, Hoffman R L and Wager J F 2006 Transparent ring oscillator based on indium gallium oxide thin-film transistors *Solid State Electron.* **50** 500–3
[7] Schleife A, Rödl C, Fuchs F, Furthmüller J and Bechstedt F 2009 Optical and energy-loss spectra of MgO, ZnO and CdO from *ab initio* many-body calculations *Phys. Rev.* B **80** 035112
[8] Makino T, Tamura K, Chia C H, Segawa Y, Kawasaki M, Ohtomo A and Koinuma H 2002 Optical properties of ZnO:Al epilayers: observation of room-temperature many-body absorption-edge singularity *Phys. Rev.* B **65** 121201
[9] Sernelius B E, Berggren K-F, Jin Z-C, Hamberg I and Granqvist C G 1988 Band-gap tailoring of ZnO by means of heavy Al doping *Phys. Rev.* B **37** 10244–8
[10] Major S, Banerjee A and Chopra K L 1983 Highly transparent and conducting indium-doped zinc oxide films by spray pyrolysis *Thin Solid Films* **108** 333–40
[11] Özgür U, Alivov Y I, Liu C, Teke A, Reshchikov M A, Doğan S, Avrutin V, Cho S-J and Morkoç H 2005 A comprehensive review of ZnO materials and devices *J. Appl. Phys.* **98** 041301
[12] Jefferson P H, Hatfield S A, Veal T D, King P D C, McConville C F, Zúñiga-Pérez J and Muñoz-Sanjosé V 2008 Bandgap and effective mass of epitaxial cadmium oxide *Appl. Phys. Lett.* **92** 022101
[13] Ramirez A P 2007 Oxide electronics emerge *Science* **315** 1377–8
[14] Tsukazaki A, Ohtomo A, Kita T, Ohno Y, Ohno H and Kawasaki M 2007 Quantum Hall effect in polar oxide heterostructures *Science* **315** 1388–91
[15] Ohtomo A and Tsukazaki A 2005 Pulsed laser deposition of thin films and superlattices based on ZnO *Semicond. Sci. Tech.* **20** S1–12
[16] Sadofev S, Blumstengel S, Cui J, Puls J, Rogaschewski S, Schäfer P, Sadofyev Y G and Henneberger F 2005 Growth of high-quality ZnMgO epilayers and ZnO/znmgo quantum well structures by radical-source molecular-beam epitaxy on sapphire *Appl. Phys. Lett.* **87** 091903

[17] Sadofev S, Blumstengel S, Cui J, Puls J, Rogaschewski S, Schäfer P and Henneberger F 2006 Visible band-gap ZnCdo heterostructures grown by molecular beam epitaxy *Appl. Phys. Lett.* **89** 201907
[18] Shigemori S, Nakamura A, Ishihara J, Aoki T and Temmyo J 2004 $Zn_{1-x}Cd_xO$ film growth using remote plasma-enhanced metalorganic chemical vapor deposition *Japan. J. Appl. Phys.* **43** L1088–90
[19] Schmidt R *et al* 2003 Dielectric functions (1 to 5 eV) of wurtzite $Mg_xZn_{1-x}O$ ($\leqslant$0.29) thin films *Appl. Phys. Lett.* **82** 2260–2
[20] Makino T, Segawa Y, Kawasaki M, Ohtomo A, Shiroki R, Tamura K, Yasuda T and Koinuma H 2001 Band gap engineering based on $Mg_xZn_{1-x}O$ and $Xd_yZn_{1-y}O$ ternary alloy films *Appl. Phys. Lett.* **78** 1237–9
[21] Venkatachalapathy V, Galeckas A, Trunk M, Zhang T, Azarov A and Kuznetsov A Y 2011 Understanding phase separation in ZnCdo by a combination of structural and optical analysis *Phys. Rev.* B **83** 125315
[22] Martienssen W and Warlimont H (ed) 2005 *Springer Handbook of Condensed Matter and Materials Data* (Berlin: Springer)
[23] Schleife A, Fuchs F, Furthmüller J and Bechstedt F 2006 First-principles study of ground- and excited-state properties of MgO, ZnO and CdO polymorphs *Phys. Rev.* B **73** 245212
[24] Schleife A, Eisenacher M, Rödl C, Fuchs F, Furthmüller J and Bechstedt F 2010 Ab initio description of heterostructural alloys: thermodynamic and structural properties of $Mg_xZn_{1-x}O$ and $Cd_xZn_{1-x}O$ *Phys. Rev.* B **81** 245210
[25] Popescu V and Zunger A 2010 Effective band structure of random alloys *Phys. Rev. Lett.* **104** 236403
[26] Chen A-B and Sher A 1995 *Semiconductor Alloys* (New York: Plenum)
[27] Sanchez J M, Ducastelle F and Gratias D 1984 Generalized cluster description of multicomponent systems *Physica* A **128** 334–50
[28] Zunger 1994 *First-Principles Statistical Mechanics of Semiconductor Alloys and Intermetallic Compounds* (New York: Plenum) 361
[29] Sher A, van Schilfgaarde M, Chen A B and Chen W 1987 Quasichemical approximation in binary alloys *Phys. Rev.* B **36** 4279–95
[30] Caetano C, Teles L K, Marques M, Dal Pino A and Ferreira L G 2006 Phase stability, chemical bonds, and gap bowing of $In_xGa_{1-x}N$ alloys: comparison between cubic and wurtzite structures *Phys. Rev.* B **74** 045215
[31] Teles L K, Furthmüller J, Scolfaro L M R, Leite J R and Bechstedt F 2000 First-principles calculations of the thermodynamic and structural properties of strained $In_xGa_{1-x}N$ and $Al_xGa_{1-x}N$ alloys *Phys. Rev.* B **62** 2475–85
[32] Connolly J W D and Williams A R 1983 Density-functional theory applied to phase transformations in transition-metal alloys *Phys. Rev.* B **27** 5169–72
[33] Kresse G and Furthmüller J 1996 Efficient iterative schemes for *ab initio* total-energy calculations using a plane-wave basis set *Phys. Rev.* B **54** 11169–86
[34] Kresse G and Furthmüller J 1996 Efficiency of *ab-initio* total energy calculations for metals and semiconductors using a plane-wave basis set *Comput. Mater. Sci.* **6** 15–50
[35] Shishkin M and Kresse G 2006 Implementation and performance of the frequency-dependent *GW* method within the PAW framework *Phys. Rev.* B **74** 035101
[36] Gajdoš M, Hummer K, Kresse G, Furthmüller J and Bechstedt F 2006 Linear optical properties in the projector-augmented wave methodology *Phys. Rev.* B **73** 045112
[37] Blöchl P E 1994 Projector augmented-wave method *Phys. Rev.* B **50** 17953–79
[38] Kresse G and Joubert D 1999 From ultrasoft pseudopotentials to the projector augmented-wave method *Phys. Rev.* B **59** 1758–75
[39] Hobbs D, Kresse G and Hafner J 2000 Fully unconstrained noncollinear magnetism within the projector augmented-wave method *Phys. Rev.* B **62** 11556–70
[40] Hedin L 1965 New method for calculating the one-particle Green's function with application to the electron-gas problem *Phys. Rev.* A **139** A796–823
[41] Aulbur W G, Jönsson L and Wilkins J W 1999 Quasiparticle calculations in solids *Advances in Research and Applications* ed H Ehrenreich and F Spaepen (*Solid State Physics* vol 54) (New York: Academic) pp 1–218

[42] Onida G, Reining L and Rubio A 2002 Electronic excitations: density-functional versus many-body Green's-function approaches *Rev. Mod. Phys.* **74** 601–59
[43] Kohn W and Sham L J 1965 Self-consistent equations including exchange and correlation effects *Phys. Rev.* **140** A1133–8
[44] Hohenberg P and Kohn W 1964 Inhomogeneous electron gas *Phys. Rev.* **136** B864–71
[45] Hybertsen M S and Louie S G 1986 Electron correlation in semiconductors and insulators: band gaps and quasiparticle energies *Phys. Rev.* B **34** 5390–413
[46] Heyd J, Scuseria G E and Ernzerhof M 2003 Hybrid functionals based on a screened Coulomb potential *J. Chem. Phys.* **118** 8207–15
[47] Paier J, Marsman M, Hummer K, Kresse G, Gerber I C and Ángyán J G 2006 Screened hybrid density functionals applied to solids *J. Chem. Phys.* **124** 154709
[48] Schleife A *et al* 2008 *Ab-initio* studies of electronic and spectroscopic properties of MgO, ZnO and CdO *J. Korean Phys. Soc.* **53** 2811–5
[49] Schleife A, Fuchs F, Rödl C, Furthmüller J and Bechstedt F 2009 Band-structure and optical-transition parameters of wurtzite MgO, ZnO, and CdO from quasiparticle calculations *Phys. Status Solidi* B **246** 2150–3
[50] King P D C, Veal T D, Schleife A, Zúñiga-Pérez J, Martel B, Jefferson P H, Fuchs F, Muñoz-Sanjosé V, Bechstedt F and McConville C F 2009 Valence-band electronic structure of CdO, ZnO and MgO from x-ray photoemission spectroscopy and quasi-particle-corrected density-functional theory calculations *Phys. Rev.* B **79** 205205
[51] Piper L F J, DeMasi A, Smith K E, Schleife A, Fuchs F, Bechstedt F, Zúñiga-Pérez J and Muñoz-Sanjosé V 2008 Electronic structure of single-crystal rocksalt Cdo studied by soft x-ray spectroscopies and *ab initio* calculations *Phys. Rev.* B **77** 125204
[52] Preston A R H, Ruck B J, Piper L F J, DeMasi A, Smith K E, Schleife A, Fuchs F, Bechstedt F, Chai J and Durbin S M 2008 Band structure of ZnO from resonant x-ray emission spectroscopy *Phys. Rev.* B **78** 155114
[53] Schleife A, Varley J B, Fuchs F, Rödl C, Bechstedt F, Rinke P, Janotti A and Van de Walle C G 2011 Tin dioxide from first principles: quasiparticle electronic states and optical properties *Phys. Rev.* B **83** 035116
[54] Monkhorst H J and Pack J D 1976 Special points for Brillouin-zone integrations *Phys. Rev.* B **13** 5188–92
[55] Paier J, Hirschl R, Marsman M and Kresse G 2005 The Perdew–Burke–Ernzerhof exchange-correlation functional applied to the G2-1 test set using a plane-wave basis set *J. Chem. Phys.* **122** 234102
[56] Fuchs F, Furthmüller J, Bechstedt F, Shishkin M and Kresse G 2007 Quasiparticle band structure based on a generalized Kohn–Sham scheme *Phys. Rev.* B **76** 115109
[57] Schleife A, Rödl C, Fuchs F, Furthmüller J and Bechstedt F 2007 Strain influence on valence-band ordering and excitons in ZnO: an *ab initio* study *Appl. Phys. Lett.* **91** 241915
[58] Rödl C, Fuchs F, Furthmüller J and Bechstedt F 2008 Ab initio theory of excitons and optical properties for spin-polarized systems: application to antiferromagnetic MnO *Phys. Rev.* B **77** 184408
[59] Rödl C, Fuchs F, Furthmüller J and Bechstedt F 2009 Quasiparticle band structures of the antiferromagnetic transition-metal oxides MnO, FeO, CoO and NiO *Phys. Rev.* B **79** 235114
[60] Strinati G 1988 Application of the Green's functions method to the study of the optical properties of semiconductors *Riv. Nuovo Cimento* **11** 1–86
[61] Hanke W and Sham L J 1979 Many-particle effects in the optical excitations of a semiconductor *Phys. Rev. Lett.* **43** 387–90
[62] Albrecht S, Reining L, Del Sole R and Onida G 1998 Ab initio calculation of excitonic effects in the optical spectra of semiconductors *Phys. Rev. Lett.* **80** 4510–3
[63] Benedict L X, Shirley E L and Bohn R B 1998 Optical absorption of insulators and the electron–hole interaction: an *ab initio* calculation *Phys. Rev. Lett.* **80** 4514–7
[64] Rohlfing M and Louie S G 1998 Electron–hole excitations in semiconductors and insulators *Phys. Rev. Lett.* **81** 2312–5

[65] Hahn P H, Schmidt W G and Bechstedt F 2001 Bulk excitonic effects in surface optical spectra *Phys. Rev. Lett.* **88** 016402
[66] Fuchs F, Rödl C, Schleife A and Bechstedt F 2008 Efficient $O(N^2)$ approach to solve the Bethe–Salpeter equation for excitonic bound states *Phys. Rev.* B **78** 085103
[67] Dudarev S L, Botton G A, Savrasov S Y, Humphreys C J and Sutton A P 1998 Electron-energy-loss spectra and the structural stability of nickel oxide: an LSDA+U study *Phys. Rev.* B **57** 1505–9
[68] Perdew J P, Chevary J A, Vosko S H, Jackson K A, Pederson M R, Singh D J and Fiolhais C 1992 Atoms, molecules, solids and surfaces: applications of the generalized gradient approximation for exchange and correlation *Phys. Rev.* B **46** 6671–87
[69] Wang Y and Perdew J P 1991 Correlation hole of the spin-polarized electron gas, with exact small-wave-vector and high-density scaling *Phys. Rev.* B **44** 13298–307
[70] Bechstedt F, Sole R D, Cappellini G and Reining L 1992 An efficient method for calculating quasiparticle energies in semiconductors *Solid State Commun.* **84** 765–70
[71] Cappellini G, Del Sole R, Reining L and Bechstedt F 1993 Model dielectric function for semiconductors *Phys. Rev.* B **47** 9892–5
[72] Schmidt W G, Glutsch S, Hahn P H and Bechstedt F 2003 Efficient $O(N^2)$ method to solve the Bethe–Salpeter equation *Phys. Rev.* B **67** 085307
[73] Mönch W 2001 *Semiconductor Surfaces and Interfaces* (Berlin: Springer)
[74] Flores F and Tejedor C 1979 Energy barriers and interface states at heterojunctions *J. Phys. C: Solid State Phys.* **12** 731–49
[75] Tersoff J 1984 Theory of semiconductor heterojunctions: the role of quantum dipoles *Phys. Rev.* B **30** 4874–7
[76] Tejedor C and Flores F 1977 A simple approach to heterojunctions *J. Phys. C: Solid State Phys.* **11** L19–23
[77] Schleife A, Fuchs F, Rödl C, Furthmüller J and Bechstedt F 2009 Branch-point energies and band discontinuities of III-nitrides and III-/II-oxides from quasiparticle band-structure calculations *Appl. Phys. Lett.* **94** 012104
[78] Chuang S L and Chang C S 1996 $k \cdot p$ method for strained wurtzite semiconductors *Phys. Rev.* B **54** 2491–504
[79] Enderlein R and Horing N J M 1997 *Fundamentals of Semiconductor Physics and Devices* (Singapore: World Scientific)
[80] Ohtomo A, Kawasaki M, Koida T, Masubuchi K, Koinuma H, Sakurai Y, Yoshida Y, Yasuda T and Segawa Y 1998 $Mg_xZn_{1-x}O$ as a II–VI widegap semiconductor alloy *Appl. Phys. Lett.* **72** 2466–8
[81] Fritsch D, Schmidt H and Grundmann M 2006 Pseudopotential band structures of rocksalt MgO, ZnO and $Mg_{1-x}Zn_xO$ *Appl. Phys. Lett.* **88** 134104
[82] Chen J, Shen W Z, Chen N B, Qiu D J and Wu H Z 2003 The study of composition non-uniformity in ternary $Mg_xZn_{1-x}O$ thin films *J. Phys. Condens. Matter* **15** L475
[83] Lambrecht W R L, Limpijumnong S and Segall B 1999 Theoretical studies of ZnO and related $Mg_xZn_{1-x}O$ alloy band structures *MRS Int. J. Nitride Semicond. Res.* 4S1:G6.8
[84] Fan X F, Sun H D, Shen Z X, Kuo J-L and Lu Y M 2008 A first-principle analysis on the phase stabilities, chemical bonds and band gaps of wurtzite structure $A_xZn_{1-x}O$ alloys (A = Ca, Cd, Mg) *J. Phys. Condens. Matter* **20** 235221
[85] Sanati M, Hart G L W and Zunger A 2003 Ordering tendencies in octahedral MgO–ZnO alloys *Phys. Rev.* B **68** 155210
[86] Thöt R K, Sander T, Klar P J and Meyer B 2009 Photocurrent measurements of $Mg_xZn_{1-x}O$ epitaxial layers of different x *MRS Proc.* **1201** H10–33
[87] Maznichenko I V *et al* 2009 Structural phase transitions and fundamental band gaps of $Mg_xZn_{1-x}O$ alloys from first principles *Phys. Rev.* B **80** 144101
[88] Moses P G, Miao M, Yan Q and Van de Walle C G 2011 Hybrid functional investigations of band gaps and band alignments for AlN, GaN, InN and InGaN *J. Chem. Phys.* **134** 084703
[89] Weissker H-C, Hambach R, Olevano V and Reining L 2009 Interpolation between spectra satisfying sum rules *Phys. Rev.* B **79** 094102